

Thermal Insulation Properties of Hollow Y2O3:Eu Spheres Laminated with Er2O3

YanXin Dan (✉ danyanxin@nimte.ac.cn)

Technology and Engineering Center for Space Utilization Chinese Academy of Sciences

<https://orcid.org/0000-0003-0178-8795>

Atsushi Nakamura

chubu chelest

Hidetoshi Saitoh

Nagaoka University of Technology

Hua Li

Ningbo Institute of Materials Technology and Engineering Chinese Academy of Sciences: Ningbo
Institute of Industrial Technology Chinese Academy of Sciences

Research Article

Keywords: Microstructure, hollow Y2O3 sphere, Er2O3, ethylenediaminetetraacetic acid (EDTA), thermal insulation capability

Posted Date: June 24th, 2021

DOI: <https://doi.org/10.21203/rs.3.rs-646049/v1>

License:   This work is licensed under a Creative Commons Attribution 4.0 International License.

[Read Full License](#)

Abstract

Currently, hollow sphere insulating materials are of importance for applications such as energy storage and savings and cryogenic engineering. The structures are formed by single hollow spheres, which can be joined, for example, by sintering. In this study, a 15 wt% Er-EDTA complex aqueous solution in which hollow Y_2O_3 spheres were mixed was used as the deposition body, and pencil spraying and sintering (PSS) was used to synthesize an Er_2O_3 hollow Y_2O_3 sphere composite film on a polished Si substrate. The structure of the composite film was successfully controlled by adjusting the 15 wt% Er-EDTA solution/hollow Y_2O_3 sphere mass ratio and the jet-to-substrate distance in the PSS process. In addition, the thermal insulation capability of the films was evaluated by the thermal steady-state method. The results show that the Er_2O_3 /hollow Y_2O_3 :Eu sphere composite films have a higher thermal insulation capability at a jet-to-substrate distance of 150 mm and a mass ratio (g) of 3.5:1. For the composite films with thicknesses of 38–92 μm , cross-sectional hollow ratio of 0.8–8.7% and void ratio of 6.3–13.1%, the temperature drop due to the porous (including hollow spheres and voids) structure films at 440°C is $\Delta T_f = 47^\circ\text{C}$. This is mainly associated with the film having more complicated microstructures. Therefore, the Er_2O_3/Y_2O_3 :Eu composite film has good thermal insulation performance, and a simple preparation method for many kinds of hollow sphere films with complex structures and high porosities by using complex solutions with different compositions is provided.

1. Introduction

In recent years, hollow sphere structure materials have been developed, and compared with ordinary materials, they have light weight, low density, and large specific surface area and are characterized by high specific stiffness, the ability to absorb high amounts of energy at relatively low stress levels, the potential for noise control, vibration damping and thermal insulation, and reduced consumption of resources and environmental issues[1–4]. A combination of these different properties provides a wide range of potential multifunctional applications, especially in the automotive and aerospace industries[5]. Typical functional applications of porous materials include in insulation for furnaces, fire retardant systems, thermal-mechanical aerospace structures, etc.[6–9]. Moreover, porous materials can be classified as either open- or closed-cell based on their structural properties. Compared to open-cell structures, closed-cell structures have advantages in thermal insulation due to their load-bearing cell walls[10–13] and have received considerable attention in recent studies. For films with high thermal insulation performance, in addition to the design of porous structure films, low thermal conductivity of the material itself is important, such as for yttrium oxide (Y_2O_3) materials[14, 15].

A considerable fraction of this kind of research has been devoted to Y_2O_3 [16–23]. Previous investigations have shown that pores are of consequence in decreasing the thermal transfer of Y_2O_3 films, in which the deposited splat forms a honeycomb microstructure film that exhibits a good thermal insulation capability[16]. Furthermore, hollow Y_2O_3 spheres may be a potential candidate for thermal insulation materials by combining the low thermal conductivity of Y_2O_3 with hollow structures. In a previous study,

hollow (Y,Eu)-EDTA complex powder was obtained by the spray-drying technique, which has a morphological and compositional design ability. The results indicated that the hollow sphere form of $Y_2O_3:Eu$ with a diameter of 1–30 μm was obtained by thermal decomposition of the complex powder[24]. In a follow-up study, a spray dryer with a two-fluid nozzle was used to synthesize hollow $Y_2O_3:Eu$ spheres, in which the size of the hollow spheres could be controlled. When the sintering temperature was 600°C, a hollow sphere with uniform size, a dense shell, and high porosity was obtained[25]. By combining the advantages of the low thermal conductivity and thermal stability characteristics of the Y_2O_3 material, thermal insulation films with complicated macroscopic and microscopic pores formed by the pencil spraying and sintering (PSS) method and controllable pores derived from hollow $Y_2O_3:Eu$ spheres can be synthesized.

In this paper, Er_2O_3 /hollow $Y_2O_3:Eu$ sphere composite films were successfully synthesized using a 15 wt% Er-EDTA complex aqueous solution as a green body for joining the spheres to form interdependent structures by the PSS process. The composite films are designed to be constructed by sintered compact hollow spheres, which not only results in a closed-cell structure to ensure mechanical strength but also leads to relatively high porosity to guarantee a good thermal insulation performance. The effect of spray parameters (jet-to-substrate distance and mass ratio of the solution) on the structure of the composite films was studied, and the connection microstructure between the hollow spheres was discussed based on energy-dispersive X-ray spectroscopy (EDX). Finally, the influence of the microstructure, porosity, and number of hollow spheres on the thermal insulation capability of Er_2O_3 /hollow $Y_2O_3:Eu$ sphere composite films was studied.

2. Experimental

2.1. Materials

The EDTA precursor was complexed and decomposed at approximately 400°C[26]. For the preparation of the initial solution, we used a 15 wt% Er-EDTA (or EDTA·Er·H ammonia) complex aqueous solution (chelated with Er^{3+} iron, Chubu Chelest Co., Ltd.) as a green body (or deposition body), and the hollow raw materials (EDTA·(Y,Eu)·H, supplied by Chubu Chelest Co., Ltd.) were placed in a furnace and heated to 100°C at a rate of 5°C/min. After holding at 100°C for 10 min, the samples were heated to 250, 450, and 600°C at rates of 2.5, 0.33, and 1.25°C/min, respectively. After holding at 600°C for 4 h, hollow beads of $Y_2O_3:Eu$ phosphor spheres were finally obtained. Figure 1 shows the properties of the calcined hollow $Y_2O_3:Eu$ spheres. The hollow $Y_2O_3:Eu$ spheres have good sphericity. Furthermore, the inner structures of $Y_2O_3:Eu$ in Fig. 1(a) show many microscopic pores, which will form pores in $Y_2O_3:Eu$ ceramics and guarantee high porosity. As shown in Fig. 1(b), only the cubic Y_2O_3 phase exists in the calcined $Y_2O_3:Eu$. As shown in Fig. 1(c), the mean particle size of the calcined $Y_2O_3:Eu$ is 10.26 μm , the distribution is uniform, and this material will be beneficial to the fabrication of green bodies due to the suitable particle size distribution. Moreover, the fluorescent agent Eu was added to determine whether the hollow spheres were uniformly present in the subsequent film preparation.

Table 1

Experimental conditions for composite film produced from 15wt% Er-EDTA/hollow $Y_2O_3:Eu$ spheres with different mass-concentration ratios of the solution(g) and jet-to-substrate distances(mm).

No.	Mass ratio (g) (15wt% Er-EDTA: $Y_2O_3:Eu$)	Jet-to-substrate distances(mm)
(1) / (4)	6.9 : 1	
(2) / (5)	5.2 : 1	150 / 200
(3) / (6)	3.5 : 1	

2.2. Preparation of the Er_2O_3 /hollow $Y_2O_3:Eu$ composite films

Er_2O_3 /hollow $Y_2O_3:Eu$ composite films were prepared using the following procedure. First, a certain amount of hollow $Y_2O_3:Eu$ spheres (calcined) were dispersed in a 15 wt% Er-EDTA complex aqueous solution for 20 min under ultrasonic agitation. To investigate the effect of hollow spheres on the thermal insulation properties of the ceramic samples and optimize the content of hollow spheres in the layers, different spray parameters were used to prepare the films, and the details are listed in Table 1. Figure 2 shows the spray equipment (SB1060, DENKEN-HIGHDENTAL Co., Ltd., Japan) used for deposition of the Er_2O_3 /hollow $Y_2O_3:Eu$ sphere composite solution on a Si ($50 \times 50 \times 0.5 \text{ mm}^3$) substrate after mechanical mixing of the 15 wt% Er-EDTA complex aqueous solution and calcined $Y_2O_3:Eu$. Finally, the prepared samples were heated in a high-speed heating electric furnace (SK-3050F, Motoyama Co., Ltd., Japan). To remove the binder, the ceramic films were sintered from room temperature to 450°C for 10 h at a low heating rate of $0.33^\circ\text{C}/\text{min}$ and then heated to 600°C at a rate of $1.25^\circ\text{C}/\text{min}$. After holding at 600°C for 1 h, to densify the ceramic films, a higher temperature (1000°C) was set for 20 min with a heating rate of $20^\circ\text{C}/\text{min}$ and held for 1 h. The above process is called pencil spraying and sintering (PSS). The above operation was repeated three times (approximately 0.4 g of the mixed solution of raw materials for one time) to obtain films with a certain thickness.

2.3. Thermal insulation test

Thermal insulation tests of Er_2O_3 /hollow $Y_2O_3:Eu$ sphere composite films were performed with a k-type thermocouple[16, 27], a hot plate (CHPS-170AN, AS ONE), and a data logger (midi LOGGER GL200, GRAPHTEC). A complete thermal insulation test process consisted of isothermal heating at 400°C with a dwell time of 30 min, and the data logger recorded each temperature at intervals of 0.1 s. The average value in the quasi-stationary state (between 1500 and 1800 s) of the temperature difference between the temperature T_2 on the hot plate side and temperature T_1 on the back surface of the sample was taken as

the temperature gradient ΔT for that sample ($\Delta T = T_2 - T_1$). The thermal insulation capability ΔT_f was calculated as the difference between the ΔT of each sample and the measured temperature gradient ΔT_{si} of the Si substrate ($\Delta T_f = \Delta T - \Delta T_{al}$). The test model is shown in Fig. 3. From the above, the steady-state method was applied to perform a measurement of the thermal insulation performance when the sample had reached thermal equilibrium[16, 27].

2.4. Characteristics

The phases of the various synthesized coatings were characterized by X-ray diffraction (XRD, M03XHF22, Mac Science, Kanagawa, Japan) with Cu-K α radiation over 2θ values of 10° – 90° . The hollow sphere morphology, microstructure and composition of the films (or deposition bodies) were observed using field-emission scanning electron microscopy (FE-SEM, JSM-6700F, JEOL, Japan) equipped with EDX (JED-2201-F, Japan). Secondary electron and backscattered electron (compositional) images of the synthesized composite films were acquired. All the synthesized films for cross-sectional analysis were first embedded in transparent epoxy resin and then polished with water-resistant abrasive paper. The film thickness is the average thickness of 20 transverse sections, which was estimated by analyzing the whole SEM image with the commercial software SmileView, and measurements were repeated three times. Moreover, the number of hollow spheres, hollow ratio (hollow sphere internal area ratio) and void ratio of the film were evaluated based on 2D image analysis via ImageJ software. Image analysis has been established as a reliable method for determining the pore (or void) size and morphology in synthesized films, keeping in mind its resolution limits[28–30]. Therefore, the numbers of hollow spheres (selecting an inner diameter of 0.5 μm or larger) and voids of the films were measured from the SEM images. In addition, the acquisition parameters were fixed to an image resolution of approximately 0.2 $\mu\text{m}/\text{pixel}$, and based on these conditions, a series of 5 images were recorded to obtain an accurate value.

3. Results And Discussion

3.1. Characterization of $\text{Er}_2\text{O}_3/\text{hollow Y}_2\text{O}_3:\text{Eu}$ composite films

Figure 4 shows photographs of the composite films of $\text{Er}_2\text{O}_3/\text{hollow Y}_2\text{O}_3:\text{Eu}$ spheres with a mass ratio (g) of 3.5:1 deposited on Si substrates at different jet-to-substrate distances of 150 mm (Fig. 4(3)) and 200 mm (Fig. 4(6)) by the PSS process. At a spray distance of 150 mm, the deposition layers are in the form of concavo-convex deposits on the substrate surface. Compared to sample (3), the surface of sample (6) is more uniform. This may be due to the larger spray angle, which helps the suspension solution (or hollow spheres) be deposited more dispersedly on the substrate. In addition, both colors are the same baby pink, which is the mixed color of Er_2O_3 (pink) and Y_2O_3 (white)[16, 31]. This color change confirms the presence of the $\text{Er}_2\text{O}_3/\text{hollow Y}_2\text{O}_3:\text{Eu}$ composite films on the substrate.

Figure 5 shows the phase compositions of sintered $\text{Er}_2\text{O}_3/\text{hollow Y}_2\text{O}_3:\text{Eu}$ sphere composite films deposited at different spray distances and mass ratios. The peaks in the XRD profiles were assigned

using International Centre for Diffraction Data (ICDD) cards as references. In Fig. 5(1)–(6), the hollow sphere composite films deposited on Si substrates only exhibit cubic crystalline phases. Furthermore, diffraction peak splitting was observed in the deposited films containing the Er-EDTA complex and Y_2O_3 ceramic (after sintering EDTA-(Y,Eu)-H), the details of which were explained in our previous report[32]. In addition, the peak intensity of the composite film phase hardly changes with changing spray conditions.

To survey the surface morphology and structure of the as-synthesized Er_2O_3 /hollow Y_2O_3 :Eu sphere composite film formed by a one-time PSS process, SEM and EDX were carried out. As depicted in Fig. 6(a), three structures were formed as follows: a fibrous ribbon structure after sintering (red dotted lines I), a flatbed layer structure (red dotted lines II), and a thin layer on the sphere wall (red dotted lines III) covering (or bonded to) the hollow sphere particles on the substrate. The elemental composition of the Er_2O_3 /hollow Y_2O_3 :Eu sphere composite film was determined using EDX. The EDX images in Fig. 6(b) confirm the existence of Er (red) and Y (green) in the composite film. Combined with the SEM and EDX images, the above three structures can be confirmed to be composed of Er. This means that the connected structure (red dotted lines I, II, and III) of the hollow spherical particles is composed of the metal oxide Er_2O_3 . Then, thick films were deposited after increasing the PSS process to three times in the following.

The surface morphology and structure of the as-synthesized samples were characterized by SEM, as shown in Figs. 7 and 8. When the jet-to-substrate distance is 150 mm, hollow Y_2O_3 spheres and smaller particles ($\approx 1 \mu m$) are uniformly deposited on the substrate (Fig. 7(1)-(3)). In particular, the surface morphology of sample (1) is more compact. The magnified images in Fig. 7(1_a)-(3_c) reveal that hollow Y_2O_3 spheres with diameters of 0.1-2 μm have a remarkable cavity, and the hollow Y_2O_3 ceramic has a good spherical shape; thus, the internal pores are retained. There are gaps between the Y_2O_3 spheres, and the distance between them is large, so the interface is not obvious. The composite films also obviously consist of smaller and larger spheres bonded between them. Furthermore, a fibrous ribbon structure was observed on the surface of the Y_2O_3 spheres at mass ratios of 5.2:1 and 3.5:1 (as shown in Fig. 7(2_b)-(3_c) with the red dotted line). When the jet-to-substrate distance was 200 mm, hollow spheres with an $\approx 6 \mu m$ diameter were uniformly deposited on the substrate, and the degree of dispersion of the hollow spheres on the surface became larger, as shown in Fig. 8(4)-(6) (compared to the jet-to-substrate distance of 150 mm). Similar to the above, a fibrous structure is also observed in Fig. 8(6_f). Additionally, the hollow sphere chains are obviously formed by Y_2O_3 spheres combining with each other, which have a high bonding strength. During the PSS process, the 15 wt% Er-EDTA complex aqueous solution is sintered by the thermal effect of the furnace and then rapidly cools and solidifies to form bonding necks between the Y_2O_3 spheres that combine them together, so deposition bodies with a certain strength are formed. Furthermore, the hollow Y_2O_3 spheres maintain good integrity during the PSS forming process, and there are still many pores (or voids) between the Y_2O_3 .

Figures 9 and 10 show cross-section SEM images of samples synthesized at different distances and mass ratios. The Er_2O_3 /hollow Y_2O_3 :Eu composite films are composed of three layers with the following

special structure: (a) a porous (or top) layer, (b) a middle layer, and (c) a bonding layer, as shown in Fig. 9(2). The reason why the composite films are three layers is that the films were deposited on the substrate by the PSS process three times under the same conditions. In addition, with the decrease in the mass ratio of the solution, the fluidity of the Er-EDTA complex aqueous solution increases, and many obvious voids form between the hollow Y_2O_3 spheres. These voids become more obvious when the mass ratio is decreased to 3.5:1 (Fig. 9(3)). The magnified images in Fig. 9(1_a) and (2_b) reveal hollow spheres constructed by interconnected dense Er_2O_3 building blocks that fill the surrounding hollow Y_2O_3 sphere architectures. Additionally, the hollow spheres obviously have a thin wall with a thickness of approximately 0.3 μm . Furthermore, in these images, the hollow structure of Y_2O_3 because of the removal of the gas during calcination is visible. However, the cross-sectional image of Fig. 9(3_c) shows a loose structure, which is due to the gaps formed after the Er-EDTA complex aqueous solution was deposited and solidified during the sintering process. It also makes connection of the composite film and substrate easier. With a jet-to-substrate distance of 200 mm, sample (5) has a looser structure in the top layer and the middle layer than sample (3), as shown in Fig. 10(5). For further characterization of the bonding layer (c) of the synthesized composite films, EDX mapping is useful, and homogeneous dispersion of Er (red) and Y (green) over the particles can be observed in Fig. 11(b). Additionally, Er is obviously mainly distributed in the bonding layer (c). Therefore, this can also prove that the higher density of the bonding layer is due to the filling of Er_2O_3 (combined with Fig. 11(a) and (b)). The denser layer of the synthesized $Er_2O_3/Y_2O_3:Eu$ composite films can be explained as shown in Fig. 12(a-d). There are four steps to form the initial deposition layer: (a) The mixed solution is sprayed on the substrate by pencil spraying. (b) The Er-EDTA solution coats the surface of the hollow spheres and the substrate, and the coated spheres are dispersed on the substrate. Then, solid-liquid equilibrium is reached in stage (c). Finally, (d) the sprayed samples are sintered, and the Er-EDTA decomposition reaction to form Er_2O_3 occurs between the hollow spheres and substrate. Therefore, due to the fluidity of the solution and gravity, a denser Er_2O_3 microstructure is formed at the bottom. Table 2 shows the results of the estimated film thickness, number of hollow spheres, hollow ratio and void ratio of $Er_2O_3/Y_2O_3:Eu$ composite films synthesized on Si substrates. Sample (1) has an average thickness of 38 μm , 67 hollow spheres, a hollow ratio (selecting a hollow diameter of 0.5 μm or larger) of 0.8%, and a void ratio of 6.3% when the jet-to-substrate distance is 150 mm. With a distance of 200 mm, sample (4) has almost the same film thickness (40 μm), hollow ratio (0.7%) and void ratio (6.4%); however, the number of hollow spheres is less than that of sample (1). The dispersion of hollow spheres can be considered to become higher when the spraying distance becomes larger. This is also obvious in the results for sample (3) and sample (6) with the same mass ratio of 3.5:1.

Table 2

Results of estimated film thickness, number of hollow spheres, hollow ratio and void ratio of Er_2O_3 /hollow Y_2O_3 :Eu sphere composite films synthesized on Si substrates.

No.	Thickness (μm)	Number of hollow spheres	Hollow ratio (%)	Void ratio (%)
(1)	38	67	0.8	6.3
(2)	51	122	6.2	9.1
(3)	92	221	8.7	13.1
(4)	40	55	0.7	6.4
(5)	69	125	3.2	12.4
(6)	73	92	3.8	8.2

These results indicate that the cooling of the substrate is important for depositing composite films with the three kinds of layers (shown in Fig. 9(2)). Such a microstructure (including voids) could improve the thermal insulation capability because hollow spheres with a loose distribution could form more pores (or deposition voids) to lower the thermal conductivity, and a more horizontal layer gap might be beneficial for resisting thermal conduction[33]. Thus, this material can be expected to be a good thermal insulation material.

3.2. Thermal insulation performance of Er_2O_3 /hollow Y_2O_3 :Eu composite films

The thermal insulation performance of Er_2O_3 /hollow Y_2O_3 :Eu composite films mainly depends on the special hollow structure and the number of hollow spheres distributed in the films. Hollow Y_2O_3 spheres could greatly suppress thermal conduction due to the presence of a large fraction of air cavities within the micrometer range, making them an ideal system for creating superinsulating materials. In this study, the thermal insulation capability was evaluated by the temperature drop across the composite films ($\Delta T = T_2 - T_1$). Figure 13 shows the recorded heating temperature curves of the heater (film surface, T_0), substrate (reference) backside (T_1), and backside of specimens synthesized with different mass ratios: (T_2) 6.9:1 and (T_3) 3.5:1.

Figure 13 shows that as the heater temperature (T_0) increases, T_1 , T_2 , and T_3 all increase. The results of the temperature data indicate that T_1 , T_2 , and T_3 become stable when the holding time at a T_0 of 440°C is longer than 20 min. The backside temperatures of all samples are lower than that of the substrate. This means that the synthesized samples contribute to decreasing the temperature of the substrate. Moreover, when the jet-to-substrate distance is 150 mm, there is an obvious distinction between sample (1) and sample (3) with increasing temperature, as shown Fig. 13(a). For a distance of 200 mm, the temperature curves of the samples ((4) and (6)) are not obviously different in Fig. 13(b). Based on the evaluation

results of the films in Table 2, the better thermal insulation capability of sample (3) than that of sample (1) can be explained as being due to the values of the number of hollow spheres, hollow ratio (%), and void ratio (%) being much higher. This is also the reason why the heating curves of sample (4) and sample (6) are not obviously different. An interesting finding is that the temperature curves of samples (3) and (6) have obvious fluctuations, but those of samples (1) and (4) are relatively stable. This thermal protective role can be due to the hollow structure and voids of the films, which form an air layer inside the deposition body, and the uneven heating of the internal (hollow spheres or voids) air results in a temperature difference, resulting in air convection. Furthermore, it also lowers the overall thermal conductivity[34]. The temperature drops across the samples ($\text{Er}_2\text{O}_3/\text{hollow Y}_2\text{O}_3:\text{Eu}$ composite films; ΔT) measured at 440°C for stable values (the so-called steady-state heat flow method[35, 36]) from 25 min to 30 min are listed in Table 3. Apparently, the thermal insulation materials play a more important role in a higher temperature environment. Moreover, the tables also show the ΔT_f values for the films and ΔT_f per micron. ΔT_f depends on the porosity (hollow spheres and voids) of the composite films. ΔT_f increases with increasing composite film porosity (hollow sphere/void ratio) from 0.8/6.3% to 8.7/13.1% at a jet-to-substrate distance of 150 mm (see Table 2). However, when the jet-to-substrate distance is 200 mm, sample (5) exhibits higher ΔT_f than sample (6) at similar film thicknesses. This can be because when the concentration of hollow sphere particles is lower at a mass ratio of 5.2:1, the capability of the surface of the hollow spheres to adhere to the solution is reduced, and more voids are formed (shown in Fig. 10(5) and (6)), thus lowering the thermal insulation temperature. When the spray parameter of the jet-to-substrate distance is 150 and 200 mm, the $\text{Er}_2\text{O}_3/\text{hollow Y}_2\text{O}_3:\text{Eu}$ composite films have porosities of 8.7/13.1% and 3.8/8.2% (samples (3) and (6)) and ΔT_f values of 47°C and 21°C , respectively, with a mass ratio (g) of 3.5:1 (shown in Table 3). Moreover, when the mass ratio (g) is 5.2:1, samples (2) and (5) exhibit similar ΔT_f (33 and 32°C) at different thicknesses of 51 and 69 μm . This means that the thickness has no obvious influence on the thermal insulation capability. This also means that the spray conditions could affect the formation of the microstructure in the films, which is beneficial for improving the thermal insulation performance. In addition, the ΔT_f per micron of the thinnest sample (2) is higher than that of the other coatings. This result can occur for several reasons. First, it could be due to the larger undulation in the outer layer, in which the hollow spheres are uniformly distributed in the top, bottom and inner layers. Second, as mentioned above, sample (2) has higher hollow (6.2%) and void (9.1%) ratios, but the structure itself also has two uniform dense layers, as evidenced in the cross-sectional SEM images (Fig. 9(2)). Finally, a number of large hollow spheres and more voids were formed and oriented along the axis parallel to the film-substrate interface, which improves the thermal transfer time, resulting in lowering of the temperature, due to the film surface being perpendicular to the heat flow in this test. From the above results, the thermal insulation capability can clearly be correlated to the total porosity if the hollow spheres and voids dominate the porous structure of the films[37]. Therefore, attainment of a high performance and the feasibility of developing thermal insulation composite films of $\text{Er}_2\text{O}_3/\text{Y}_2\text{O}_3$ hollow systems with EDTA complexes are the main advantages.

Table 3
 Temperature(ΔT) and thermal insulation temperature(ΔT_f) test results of Er_2O_3 / hollow Y_2O_3 :Eu sphere composite films synthesized on Si substrates.

No.	ΔT ($^{\circ}\text{C}$)	ΔT_f ($^{\circ}\text{C}$)	ΔT_f per micron ($^{\circ}\text{C}/\mu\text{m}$)
substrate	46	-	-
(1)	64	18	0.47
(2)	79	33	0.65
(3)	93	47	0.51
(4)	61	15	0.38
(5)	78	32	0.46
(6)	67	21	0.29

4. Conclusions

In this study, Er_2O_3 /hollow Y_2O_3 :Eu sphere composite films were successfully synthesized through a spray-deposition process without surfactants or a template process. Moreover, an experimental study was carried out on the hollow sphere systems of the deposition film structures by varying two kinds of spray parameters (mass ratio and jet-to-substrate distance) to assess their properties (number of hollow spheres, hollow ratio, void ratio, and thermal insulation capacity) and functional performance as protective layers deposited on Si substrates. The three types of layers (a: porous, b: middle, and c: binding) play a significant role in the thermal insulation capability. The Er_2O_3 /hollow Y_2O_3 :Eu sphere composite films with a thickness of 93 μm exhibit a higher ΔT_f of 47 $^{\circ}\text{C}$ at a mass ratio of 3.2:1. This idea will be expanded on and deepened in further studies.

Declarations

Acknowledgments

The authors gratefully acknowledge the raw material support by CHUBU CHELEST Co., Ltd of Japan.

References

1. Levassort F, Holc J, Ringgaard E, Bove T, Kosec M, M. Lethiecq, Fabrication modelling and use of porous ceramics for ultrasonic transducer applications, *J. Electro. Ceram.* 2007, **19**:127–139

2. Sundaram S, Colombo P, Katoh Y (2013) Selected emerging opportunities for ceramics in energy, Environment, and Transportation. *Int J Appl Ceram Technol* 10:731–739
3. Chen AN, Li M, Wu JM, Cheng LJ, Liu RZ, Shi YS, C.H. Li, Enhancement mechanism of mechanical performance (2019) of highly porous mullite ceramics with bimodal pore structures prepared by selective laser sintering. *J Alloy Comp* 776:486–494
4. Liu SS, Li M, Wu JM, Chen AN, Shi YS, Li CH (2020) Preparation of high-porosity Al₂O₃ ceramic foams via selective laser sintering of Al₂O₃ poly-hollow microspheres. *Ceram Int* 46:4240–4247
5. Fiedler T, Hosseini SMH, Belova IV, Murch GE, Öchsner A (2009) A refined finite element analysis on the thermal conductivity of perforated hollow sphere structures. *Comput Mater Sci* 47:314–319
6. Wang L, Wang Y, Sun XG, He JQ, Pan ZY, Zhou Y, Wu PL (2011) Influence of pores on the thermal insulation behavior of thermal barrier coatings prepared by atmospheric plasma spray. *Mater Des* 32:36–47
7. Boomsma K, Poulikakos D, Zwick F (2003) Metal foams as compact high performance heat exchangers. *Mech Mater* 35:1161–1176
8. Benkreira H, Khan A, Horoshenkov KV, Sustainable acoustic and thermal insulation materials from elastomeric waste residues, *Chen. Eng. Sci.* 2011, **66**: 4157–4171
9. Lu W, Zhao CY, Tassou SA (2006) Thermal analysis on metal-foam dilled heat exchangers. Part I: Metal-foam filled pipes. *Int J Heat Mass Transfer* 49:2751–2761
10. Sun ZQ, Lu C, Fan J, Yuan FL (2016) Porous silica ceramics with closed-cell structure prepared by inactive hollow spheres for heat insulation. *J Alloy Comp* 662:157–164
11. Ozcivici E, Singh RP, Fabrication and characterization of ceramic foams based on silicon carbide matrix (2005) and hollow alumino-silicate spheres. *J Am Ceram Soc* 88:3338–3345
12. Simone AE, Gibson LJ (1998) Effects of solid distribution on the stiffness and strength of metallic foams. *Acta Mater* 46:2139–2150
13. Bourret J, Michot A, Tessier-Doyen N, Nait-Ali B, Pennec F, Alzina A, Vicente J, Peyratout CS, Smith DS (2014) Thermal conductivity of very porous kaolin-based ceramics. *J Am Ceram Soc* 97:938–944
14. Kitayama M, Hirao K, Watari K, Toriyama M, Kanzaki S (2000) Thermal conductivity of β-Si₃N₄: II, effect of lattice oxygen. *J Am Ceram Soc* 83(8):1985–1992
15. Lu T, Wang T, Jia YF, Ding MM, Shi Y, Xie JJ, Lei F, Zhang L, Fan LC (2020) Fabrication of high thermal conductivity silicon nitride ceramics by pressureless sintering with MgO and Y₂O₃ as sintering additives. *Ceram Int* 46:27175–27183
16. Dan YX, Costa T, Guo ZY, Nakamura A, Komatsu K, Saitoh H (2020) Thermal barrier coatings formed by flame-spray with metal–EDTA. *J J Appl Phys* 59:075507
17. Dan YX, Zhou XL, Nakamura A, Komatsu K, Saitoh H (2020) Splat morphology and microstructure of chelate flame sprayed Er₂O₃ films. *J Ceram Soc Japan* 128(11):945–953
18. Akasaka H, Ohto M, Hasebe Y, Nakamura A, Ohshio S, Saitoh H (2012) Ytria coating synthesized by reactive flame spray process using Y-EDTA complex. *Surf Coat Technol* 205:3877–3880

19. Komatsu K, Sekiya T, Toyama A, Hasebe Y, Nakamura A, Noguchi M et al (2014) Deposition of metal oxide films from metal- EDTA complexes by flame spray technique. *J Therm Spr Technol* 23:833–838
20. Komatsu K, Shirai T, Toyama A, Iseki T, Xin DY, Costa T et al (2017) Densification of metal oxide films synthesized from metal complexes by flame spraying. *Surf Coat Technol* 325:89–97
21. Dan YX, Komatsu K, Keita K, Costa T, Ikeda Y, Nakamura A et al (2017) Heat-shock properties in yttrium-oxide films synthesized from metal-ethylenediamine tetraacetic acid complex through flame-spray apparatus. *Appl Phys A* 123:194–201
22. Komatsu K, Toyama A, Sekiya T, Shirai T, Nakamura A, Toda I et al (2017) Flame-spayed Y_2O_3 films with metal-EDTA complex using various cooling agents. *J Therm Spr Technol* 26:195–202
23. Komatsu K, Costa T, Ikeda Y, Abe K, Dan YX, Kimura T, Nakamura A, Shirai T, Saitoh H (2019) Synthesis of Y_2O_3 films on an aluminum alloy substrate using flame-spray apparatus with a H_2-O_2 flame. *Int J Appl Ceram Technol* 16(1):254–263
24. Nakamura A, Nambu N, Kawahara K, Ohshio S, Saitoh H (2003) $Y_2O_3:Eu$ red phosphor powder synthesized with EDTA complexes. *J Ceram Soc Japan* 111:142–146 (in Japanese)
25. Nakamura A, Nambu N, Saitoh H, Effect of boron concentration in $Y_2O_3:(Eu,B)$ phosphor on luminescence property (2005) *Sci Tech Adv Mater* 6:210–214
26. Komatsu K, Shirai T, Toyama A, Iseki T, Xin DY, Costa T, Nakamura A, Li Y, Ohshio S, Muramatsu H, Saitoh H (2017) Densification of metal oxide films synthesized from metal complexes by flame spraying. *Surf Coat Tech* 325:89–97
27. Sekine M, Sonoya K, Nakamura M (2015) Assessment of the properties about thermal sprayed coatings for the thermal barrier applied to the head of piston of internal-combustion engine. *J Soc Mech Eng* 2(1):14–00380
28. Kulkarni A, Wang Z, Nakamura T, Sampath S, Golland A, Herman H, Allen J, Ilavsky J, Long G, Frahm J, Steinbrech RW (2003) Comprehensive microstructural characterization and predictive property modeling of plasma-sprayed zirconia coatings. *Acta Mater* 51:2457–2475
29. Hao D, Jae Heyg S, Soo Wahn L (2005) Study on porosity of plasma-sprayed coatings by digital image analysis method. *J Therm Spray Technol* 14:453–461
30. Akasaka H, Ohto M, Hasebe Y, Nakamura A, Ohshio S, Saitoh H (2011) Ytria coating synthesized by reactive flame spray process using Y-EDTA complex. *Surf Coat Technol* 205(13–14):3877–3880
31. Adachi G, Imanaka N (1998) The binary rare-earth oxides. *Chem Rev* 98(4):1479–1514
32. Komatsu K, Sekiya T, Toyama A, Shirai T, Nakamura A, Ohshio S, Toda L, Muramatsu H, Saitoh H (2016) Synthesis of $(Y, Er)_2O_3$ films from multiple-nuclei $EDTAi\frac{1}{2}Y(Y, Er)i\frac{1}{2}H$ complexes by flame spray method. *J J Therm Spr Soc* 57:70–74
33. Lima RS, Marple BR (2008) Toward highly sintering-resistant nanostructured $ZrO_2-7\text{ wt}\% Y_2O_3$ coatings for TBC applications by employing differential sintering. *J Therm Spr Technol* 17:846–852

34. Pakdel E, Naebe M, Kashi S, Cai ZX, Xie WJ, Yuen ACY, Montazer M, Sun L, Wang XG (2020) Functional cotton fabric using hollow glass microspheres: Focus on thermal insulation, flame retardancy, UV-protection and acoustic performance. *Prog Org Coat* 141:105553
35. Zhang YJ, Hao SR, Yu ZW, Fang JT, Zhang JN, Yu XM (2018) Comparison of test methods for shallow layered rock thermal conductivity between in situ distributed thermal response tests and laboratory test based on drilling in northeast China. *Energy Build* 173:634–648
36. Kerschbaumer RC, Stieger S, Gschwandl M, Fasching M, Lechner B, Meinhart L, Hildenbrandt J, Schrittester B, Fuchs PF, Berger GR, Friesenbichler W (2019) Comparison of steady-state and transient thermal conductivity testing methods using different industrial rubber compounds. *Polym Testing* 80:106121
37. Bao Y, Kang QL, Ma JZ (2017) C.Liu, Monodisperse hollow TiO_2 spheres for thermal insulation materials: Template-free synthesis, characterization and properties. *Ceram Inter* 43:8596–8602

Figures

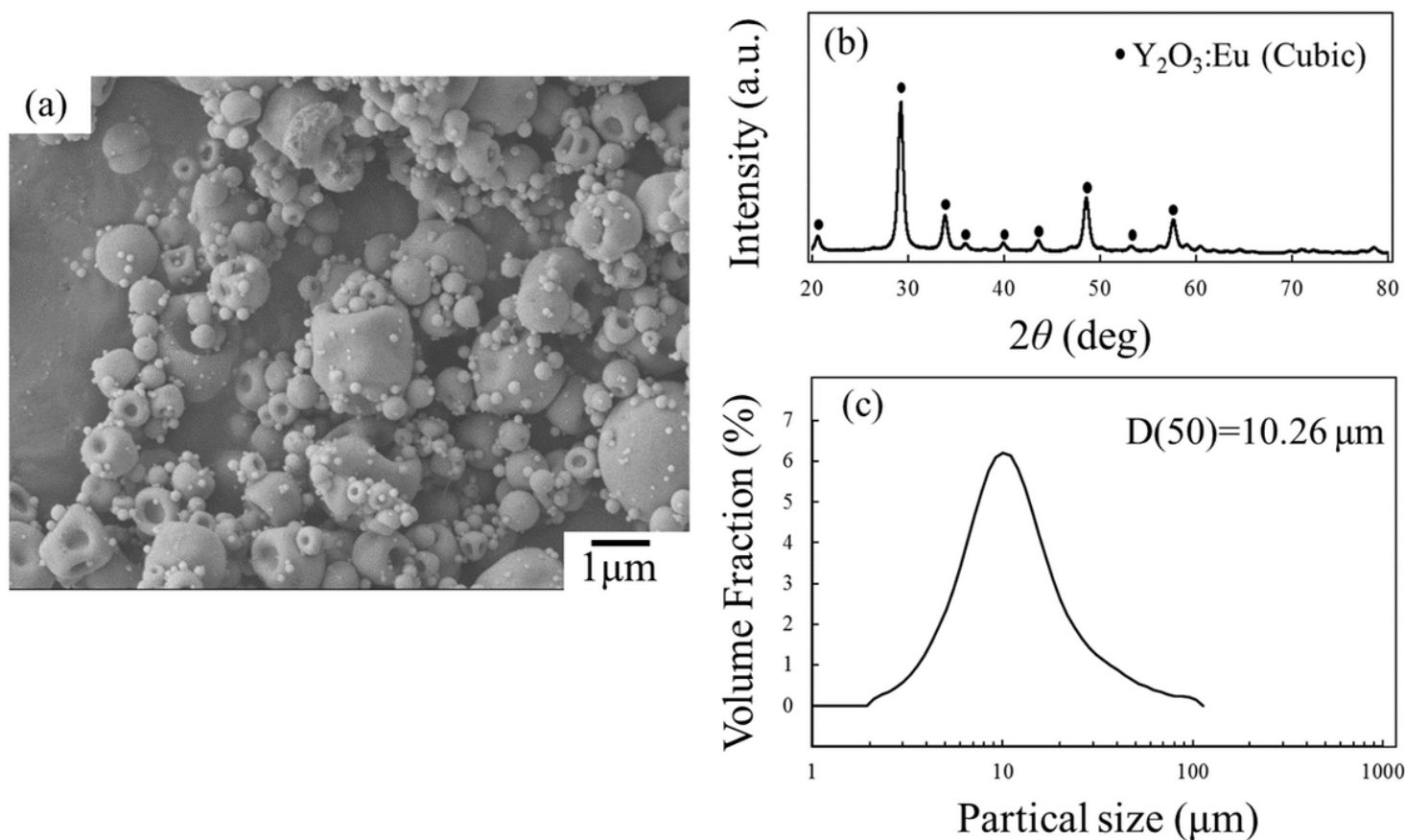


Figure 1

(a) SEM micrographs,(b) phase composition and (d) particle size distribution of EDTA(Y,Eu)H calcined into Y₂O₃:Eu.

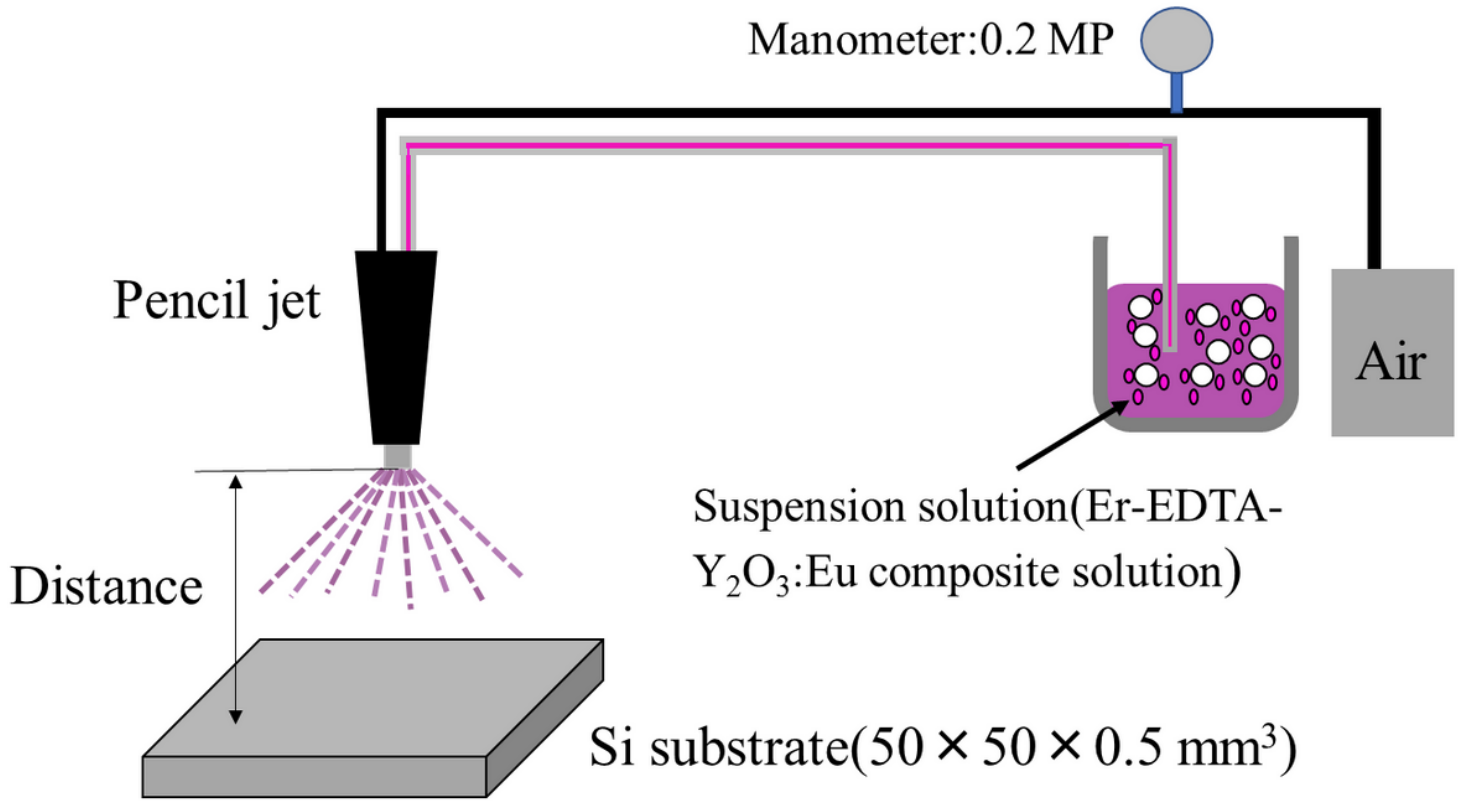
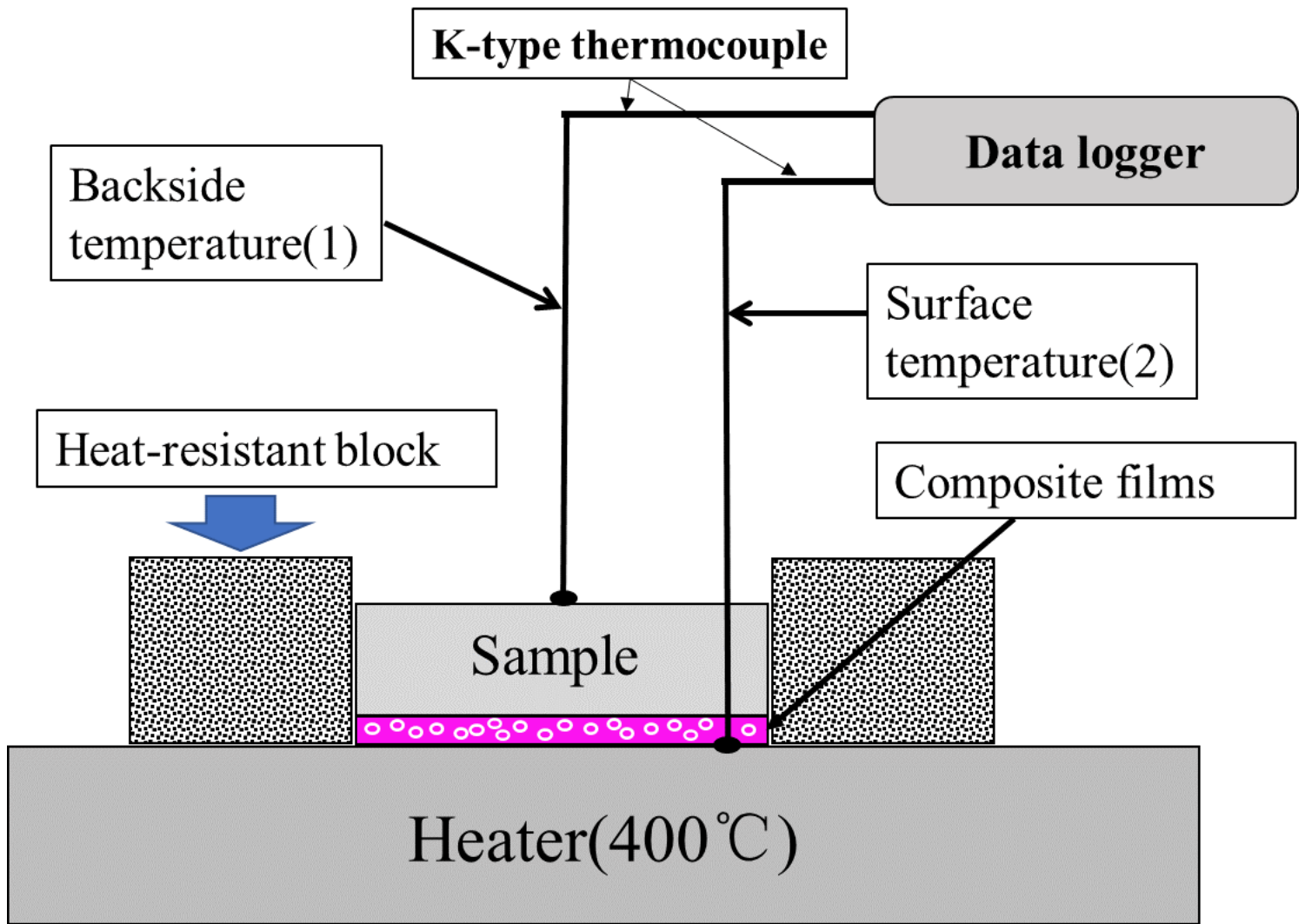


Figure 2

Schematic of the solution spray setup for deposition of the Er-EDTA/hollow Y₂O₃:Eu sphere composite solution on a Si substrate.



$$\Delta T (^{\circ}\text{C}) = \text{Temperature}(2) - \text{Temperature}(1)$$

Figure 3

Schematic diagram of the thermal insulation capability test.

(3)



(6)



— 2 cm

Figure 4

Photographs of the Er_2O_3 / hollow $\text{Y}_2\text{O}_3:\text{Eu}$ sphere composite films deposited on Si substrates.

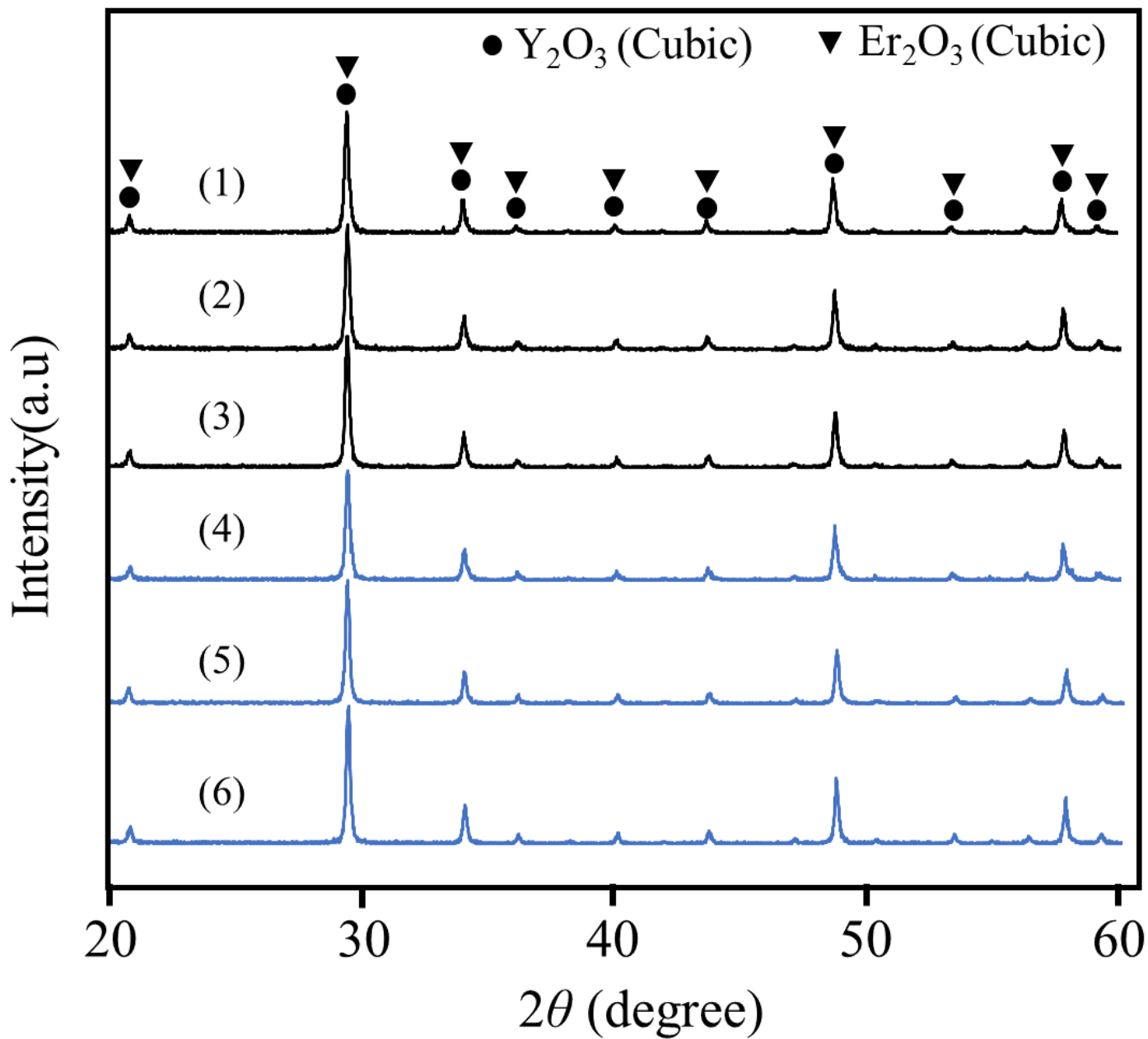


Figure 5

Phase compositions of the Er_2O_3 /hollow $Y_2O_3:Eu$ sphere composite films synthesized at different jet-to-substrate distances: (1)-(3) 150 mm; (4)-(6) 200 mm.

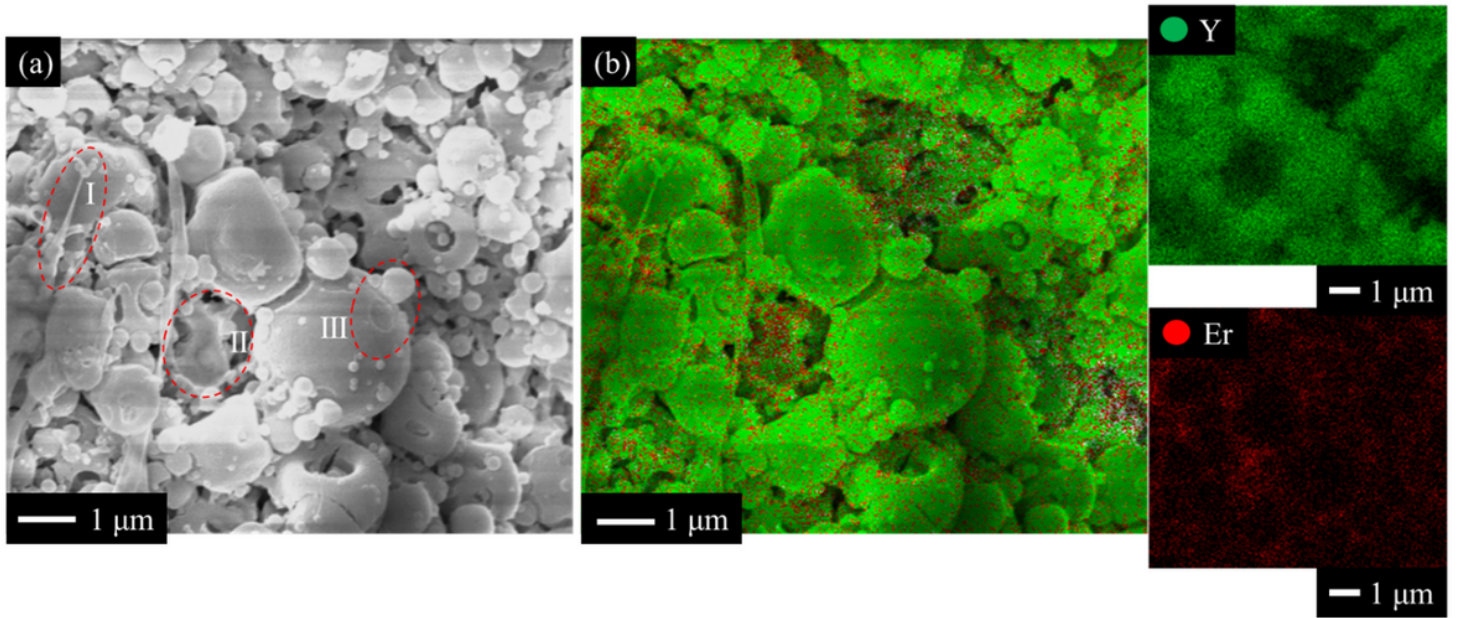


Figure 6

(a) Surface SEM image of a synthesized $\text{Er}_2\text{O}_3/\text{hollow Y}_2\text{O}_3:\text{Eu}$ sphere composite film, (b) Elemental mapping images of the $\text{Er}_2\text{O}_3/\text{hollow Y}_2\text{O}_3:\text{Eu}$ sphere composite film.

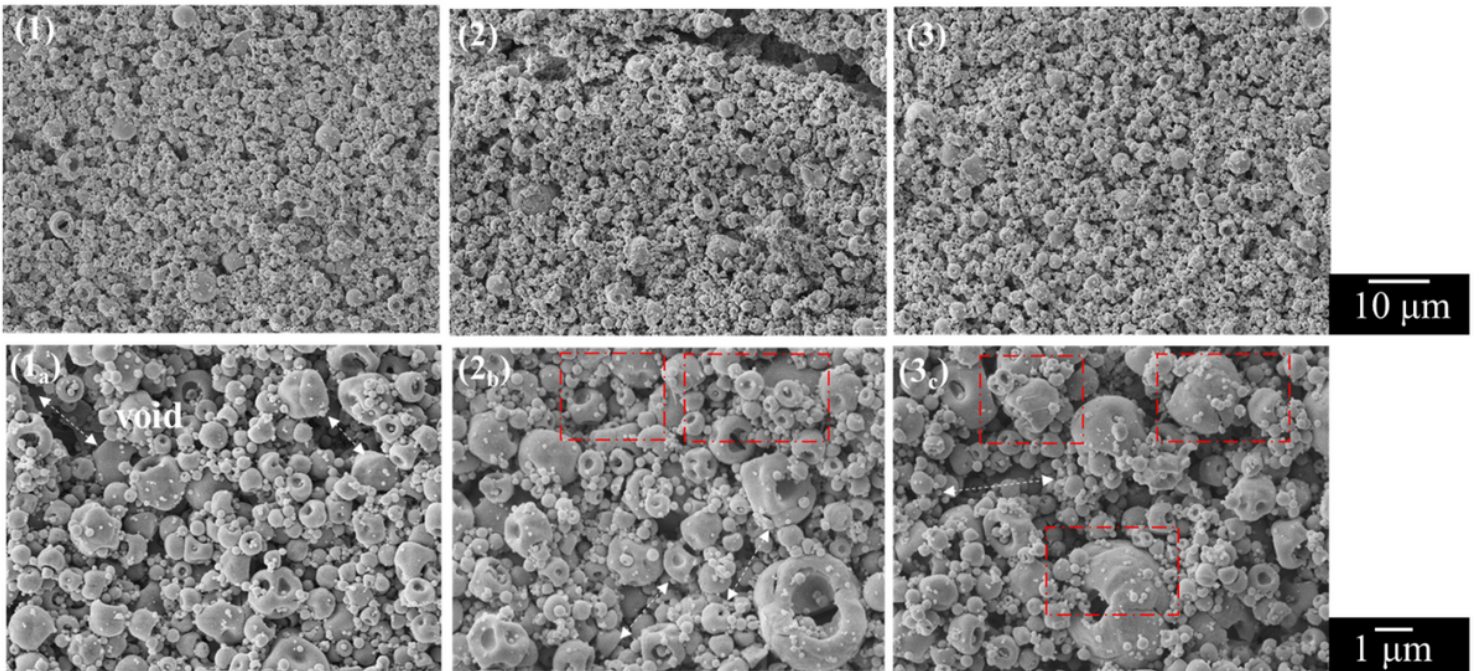


Figure 7

Surface SEM images of $\text{Er}_2\text{O}_3/\text{Y}_2\text{O}_3:\text{Eu}$ composite films ((1)-(3)), and higher magnification images of $\text{Er}_2\text{O}_3/\text{hollow Y}_2\text{O}_3:\text{Eu}$ sphere composite films ((1a)-(3c)) synthesized at the jet-to-substrate distance of 150mm.

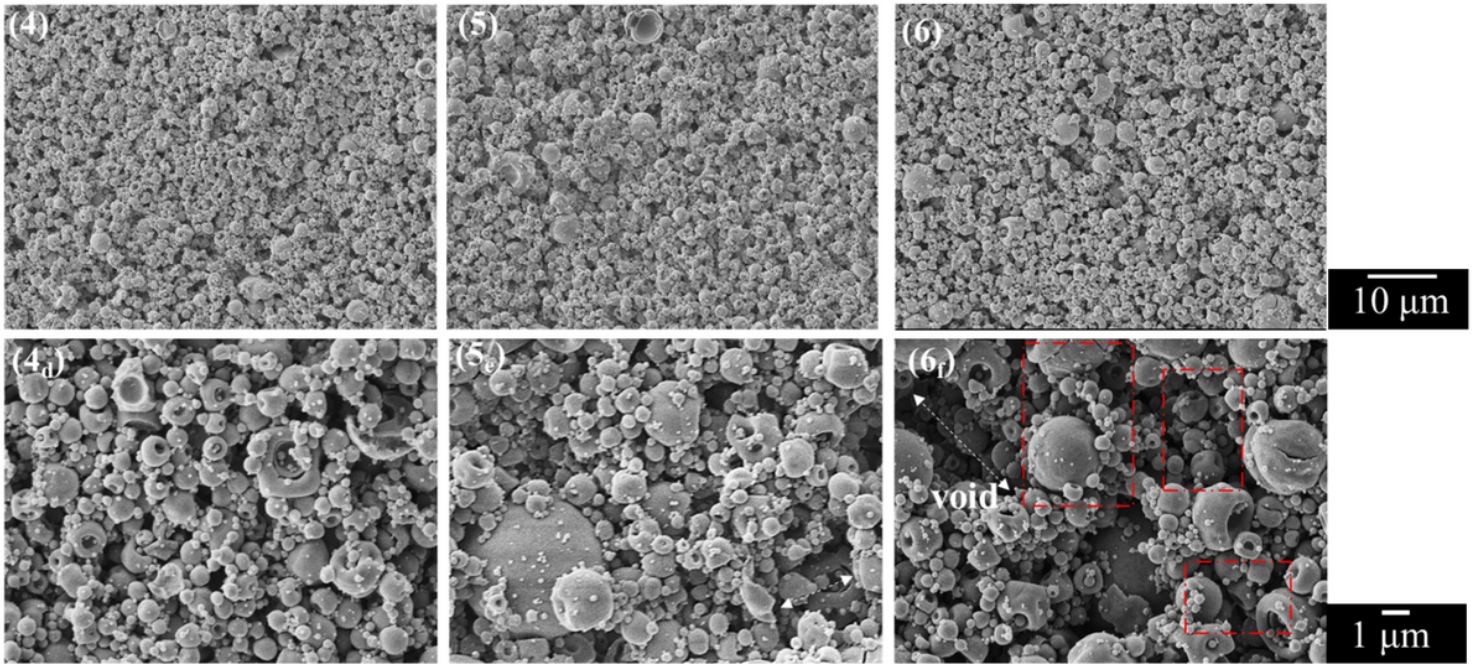


Figure 8

Surface SEM images of Er₂O₃/ Y₂O₃:Eu composite films((4)-(6)), and higher magnification images of Er₂O₃/ hollow Y₂O₃:Eu sphere composite films((4a)-(6a)) synthesized at the jet-to-substrate distance of 200mm.

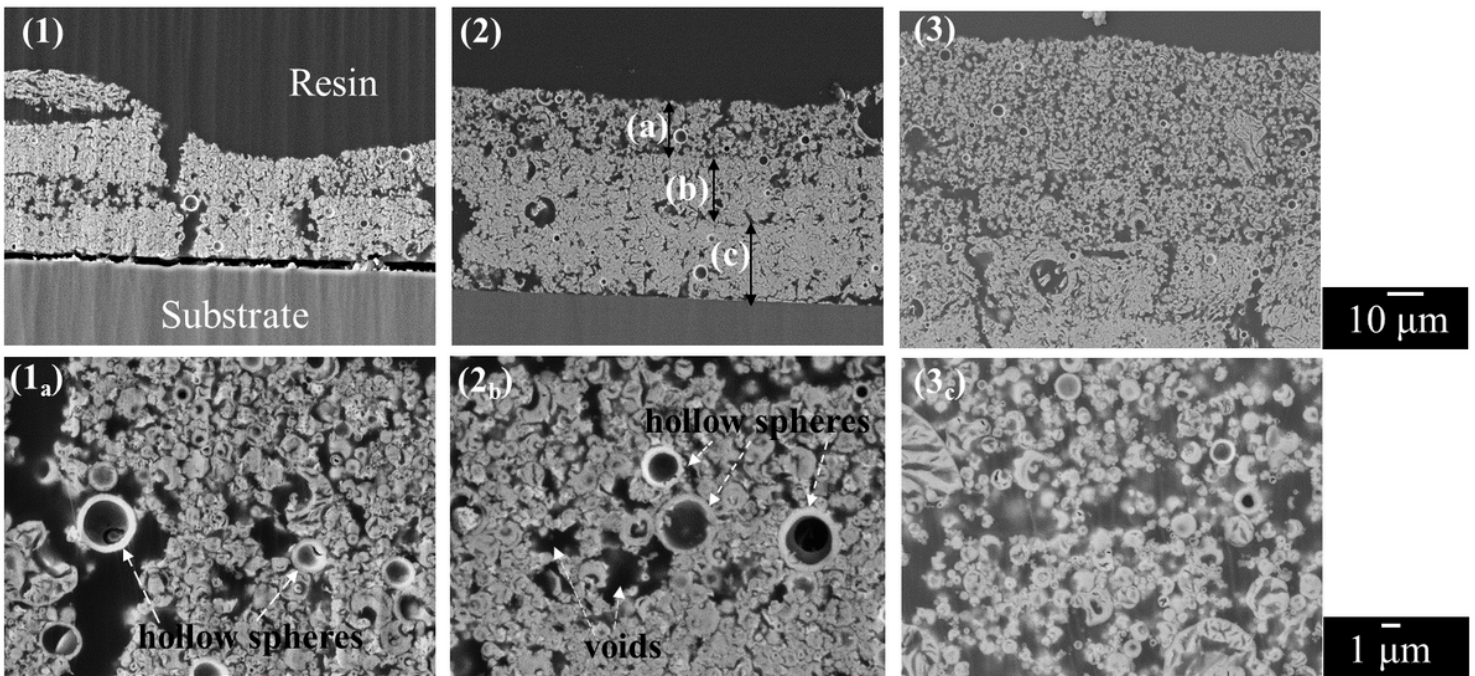


Figure 9

Cross-section SEM images of Er₂O₃/ hollow Y₂O₃:Eu sphere composite films((1)-(3)), and higher magnification images of Er₂O₃/ hollow Y₂O₃:Eu sphere composite films((1a)-(3a)) synthesized at the jet-

to-substrate distance of 150 mm.

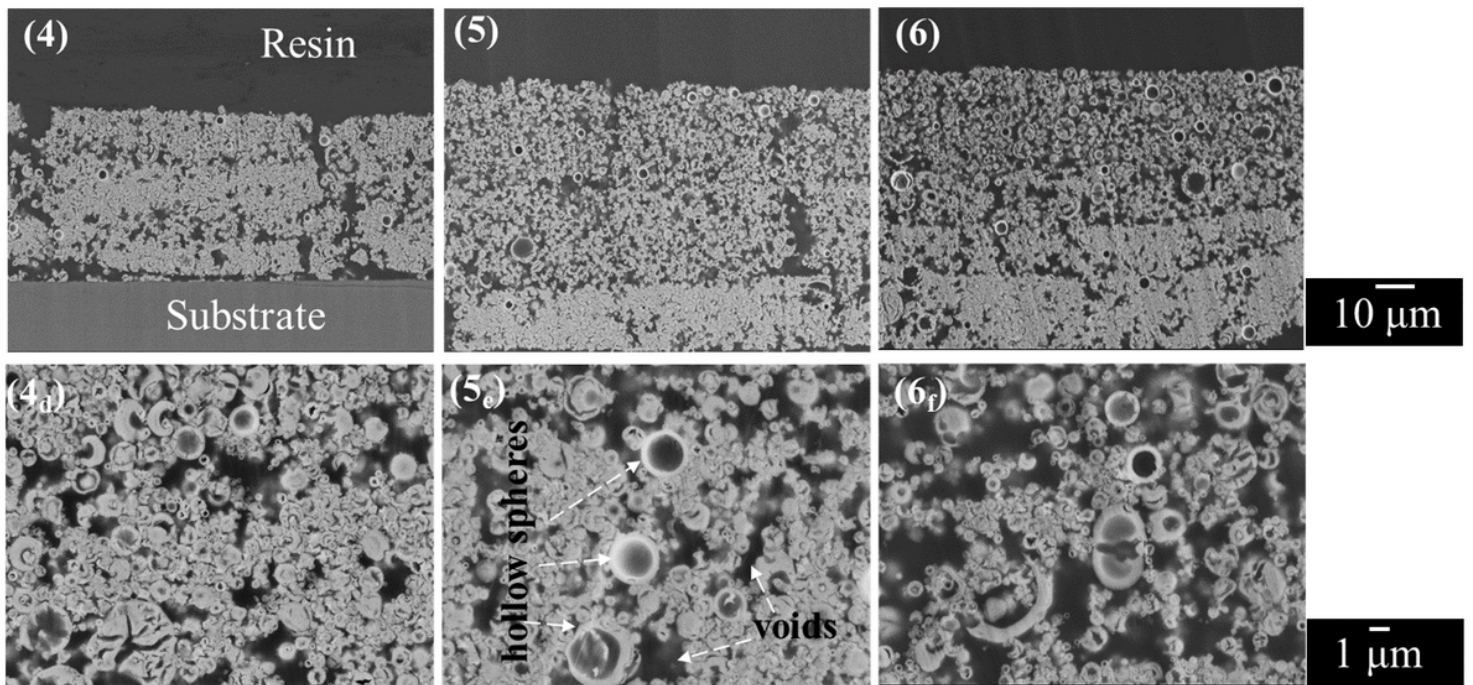


Figure 10

Cross-section SEM images of Er₂O₃/hollow Y₂O₃:Eu sphere composite films((4)-(6)), and higher magnification images of Er₂O₃/hollow Y₂O₃:Eu sphere composite films((4d)-(6f)) synthesized at the jet-to-substrate distance of 200 mm.

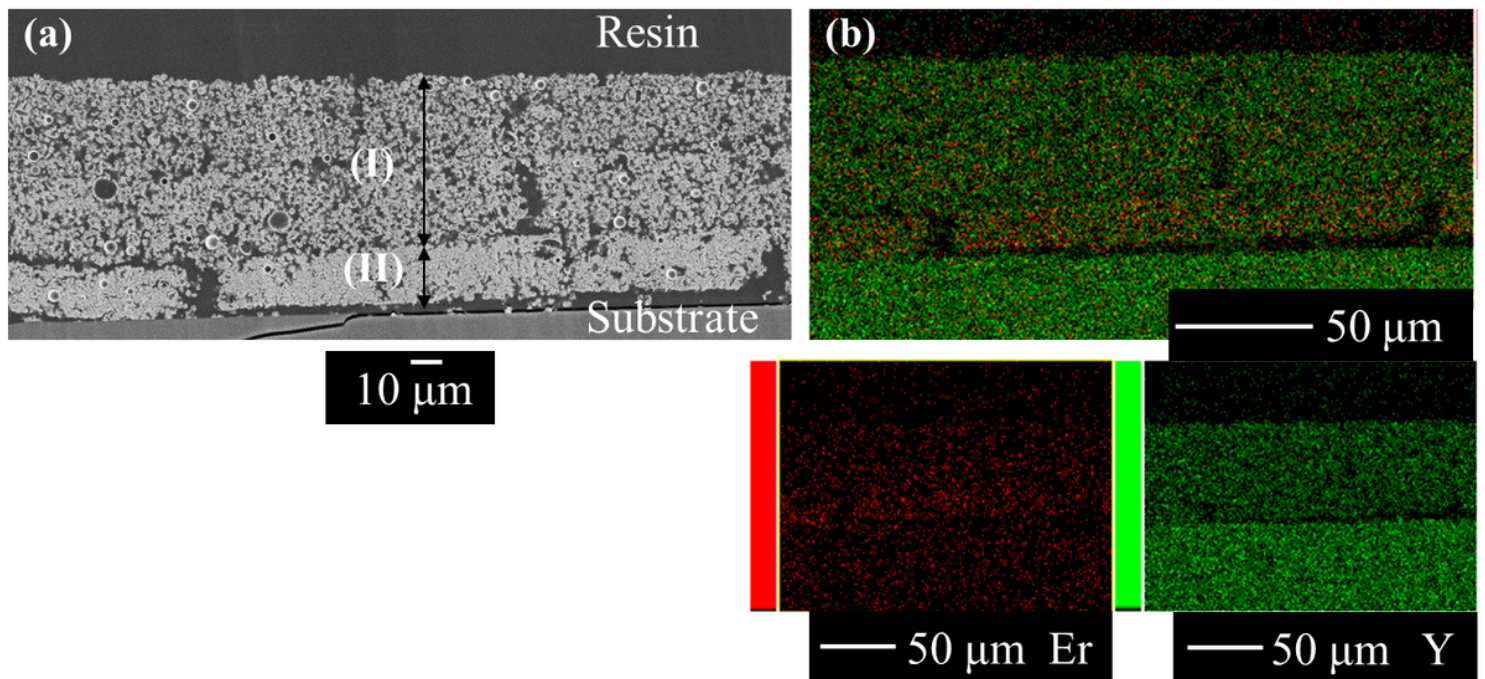


Figure 11

(a) Cross-section SEM images of synthesized Er₂O₃/ hollow Y₂O₃:Eu sphere composite films(sample 5), and (b) elemental mapping images of the region.

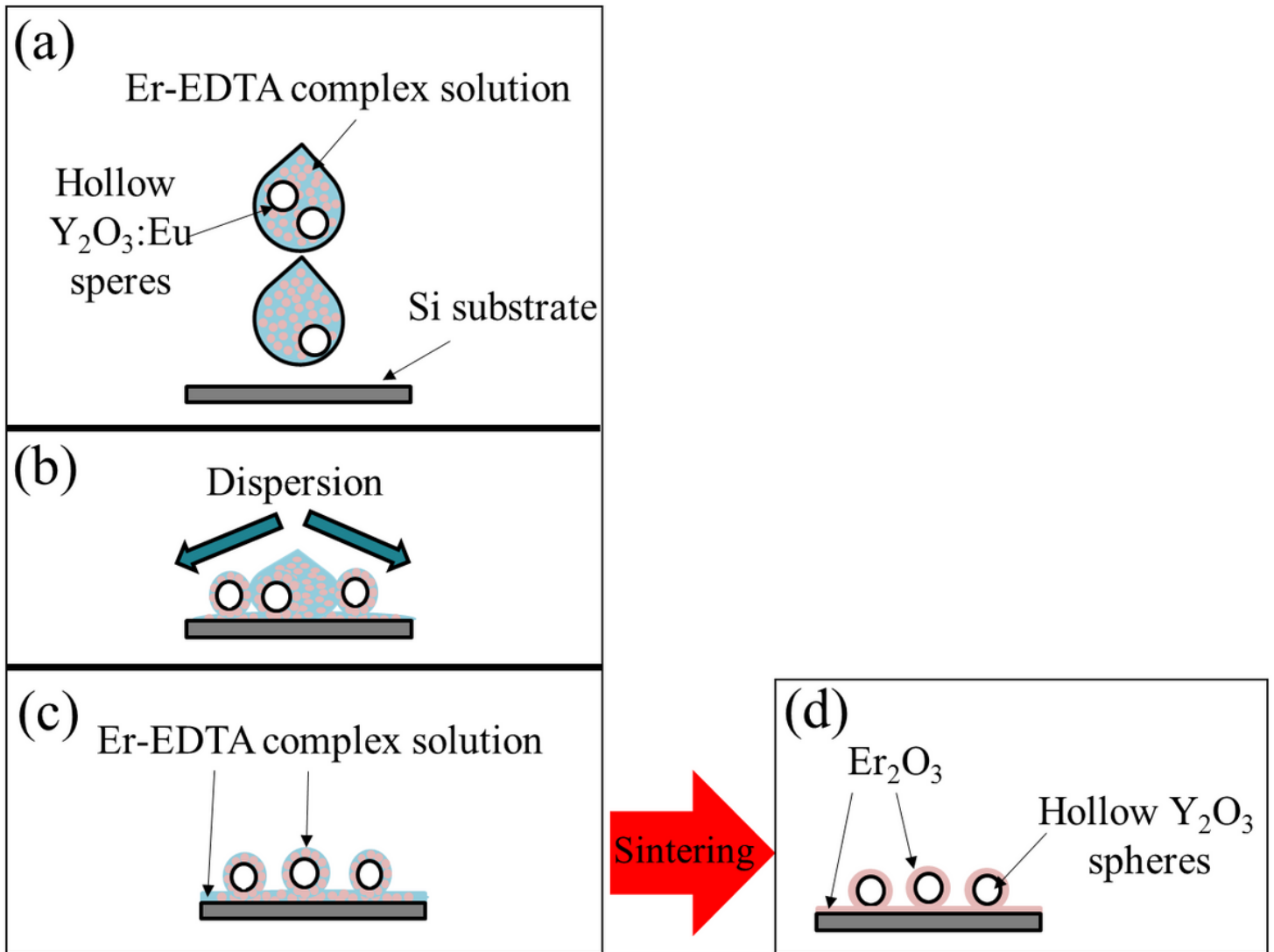


Figure 12

Flow schematic diagram of the composite film synthesis.

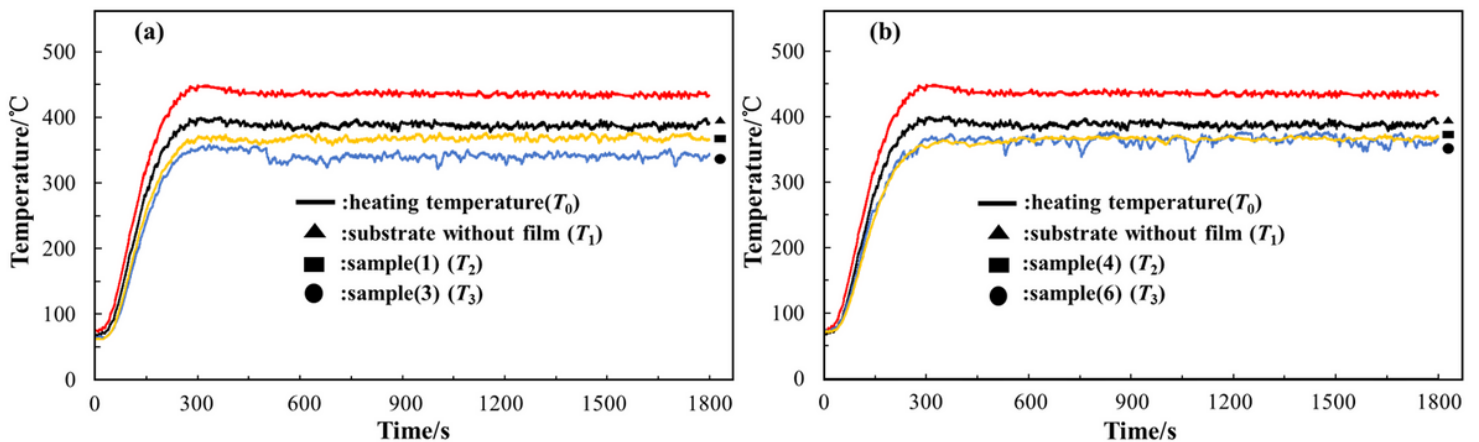


Figure 13

Heating temperature curves of the heater (T_0), substrate without a film (T_1), and backside of samples synthesized with different mass ratios: (T_2) 6.9:1, (T_3) 3.5:1. Jet-to-substrate distance: (a) 150 mm, (b) 200 mm.